Journal of Materials Chemistry A

ROYAL SOCIETY OF CHEMISTRY

PAPER

View Article Online
View Journal | View Issue

Cite this: J. Mater. Chem. A, 2020, 8, 21812

Self-healable transparent polymer/salt hybrid adhesive *via* a ternary bonding effect†

Yuanyuan Zhang, [a] Ke Zhang,[b] Xuanhua Li, *[a] Tong Li, [b] Qian Ye, [a] Li-Li Tan[a] and Bingqing Wei *[c]

Received 16th July 2020
Accepted 30th September 2020

DOI: 10.1039/d0ta06935c

rsc.li/materials-a

Tremendous attention has been focused on the design and fabrication of intrinsic self-healing materials in recent years; however, the fabrication of self-healing materials with high transparency and high adhesion strength is still a challenge. Here, we develop a novel transparent self-healing adhesive with multiple functions by simply blending poly(2-ethyl-2-oxazoline) (PEOZ), poly(4-hydroxy styrene) (PHS), and $CaCl_2$, and discover that the anion Cl^- also plays a significant role in accelerating the self-healing process by anion–ligand coordination in the form of hydrogen bonding, which has been seriously neglected in previous work. Unlike the common single metal–ligand coordination approach, the enhancement of self-healing results from novel co-existing ternary bridging bonds: metal–ligand coordination, ionic bond, and anion coordination. The universality of the new concept has been verified with other typical soluble salts $MgCl_2$, NaCl, and $Ca(NO_3)_2$, providing a new dimension in the comprehension of the self-healing mechanisms. As a result, the hybrid shows outstanding multifunctional performance compared with the most recently published self-healable adhesives taking into consideration the transparency (T_{550} = 98.9%), adhesion strength (2.57 MPa), and self-healing efficiency (91%), enabling its application as an optical material, an adhesive and also a conservation material for cultural heritage.

Introduction

Inspired by the biological world, self-healing materials have attracted growing interest since the past decade and have yielded fruitful results.[1–5] Self-healing materials are classified as extrinsic- and intrinsic-healing materials based on their fashion of healing. Materials that heal extrinsically encapsulate healing agents or nanoparticles, which are released once the material is scratched and move to the fracture to repair the damage. Materials that heal intrinsically restore the damages by reforming or exchanging the interactions within the network. Typically, intrinsic healing systems are designed with either non-covalent interactions, for instance, van der Waals forces,[1] host–guest interactions,[6] hydrogen bonding,[7–10] halogen bonding,[11] and π–π stacking interaction,[12–14] or chemical covalent bonds including metal–ligand coordination,[2,15–17] acylhydrazone bonds,[18] Diels–Alder reactions,[19,20] boronic esters,[21,22] and disulfide bonds.[23] In recent years, self-healing systems constructed by doubly dynamic connections demonstrate rapid self-healing and high mechanical strength.[24–27] In terms of the intrinsic self-healable coatings and films, several exquisite synthetic structures are employed in the form of backbones or side chains, for instance, polyaniline (PANI),[28] polydimethylsiloxane (PDMS),[9,29] polyurethane (PU),[7] polyethylenimine (PEI),[30] polyimine,[31] catechol,[32] poly(vinyl alcohol) (PVA),[33] and ureidopyrimidinone (UPy).[34,35] Self-healable adhesives have also attracted attention recently.[36,37] However, the fabrication of self-healing materials with both high transparency and high adhesion strength is still a challenge.

Among the self-healing mechanisms mentioned above, metal–ligand coordination has been deeply studied in recent years.[38] Several metal salts, especially salts of transition metals, show excellent coordination strength and have been widely adopted in the fabrication of self-healing materials as the cross-linker between the functional groups of polymers. Bode and coworkers and the group of Bao have discovered that the interaction strength of the anions on metal ions influences the self-healing behavior.[17,39,40] However, the interaction of salt anions with the polymer matrix has not been reported. In this study, we discovered that the anion also interacts with the polymer and participates in the self-healing process by anion coordination.

Herein, a transparent hybrid material, which self-heals in a wet environment, is proposed based on poly(2-ethyl-2-oxazoline) (PEOZ), poly(4-hydroxy styrene) (PHS), and $CaCl_2$

[a]State Key Laboratory of Solidification Processing, Center for Nano Energy Materials, School of Materials Science and Engineering, Northwestern Polytechnical University, Xi'an, 710072, China. E-mail: lixh32@nwpu.edu.cn

[b]Department of Engineering Mechanics, State Key Laboratory of Structural Analysis for Industrial Equipment, Dalian University of Technology, Dalian, 116024, China

[c]Department of Mechanical Engineering, University of Delaware, Newark, DE19716, USA. E-mail: weib@udel.edu

† Electronic supplementary information (ESI) available. See DOI: 10.1039/d0ta06935c

salt. The preparation procedures are relatively simple, and all of the ingredients are commercially available. Ca^{2+} has been reported with moderate coordination ability with ligands[38,41,42] and does not change the color of the polymer matrix compared with other common metal cations like Cu^{2+} or Fe^{3+} for self-healing. The resulting hybrid material illustrates a healing efficiency of more than 90% in tensile strength. The material also shows remarkable adhesion ability in both humid and ambient environments. Most importantly, it was found that the addition of the $CaCl_2$ salt into the hybrid plays a vital role in promoting the self-healing rate. Theoretical simulations and experimental results reveal that both the cation and the anion of $CaCl_2$ work as the connectors between PEOZ and PHS (Scheme 1). Different from that the combination of two orthogonal dynamic behaviors provides a dual dynamism to the reconnection of the self-healing system;[43] in our study, the resulting system accelerates the self-healing process by a ternary bonding effect. Moreover, it is transparent in the range of visible light, capable of mechanical damage recovery, and adheres to different substances, which can be beneficial in various applications, especially in the conservation of cultural heritage.

Experimental

Materials

Poly(2-ethyl-2-oxazoline) (PEOZ, $M_w \approx 200\,000$ g mol^{-1}) was purchased from Alfa Aesar (China) Co. Ltd. Poly(4-hydroxy styrene) (PHS) with $M_w \approx 11\,000$ g mol^{-1} was purchased from Sigma-Aldrich Inc. *N*,*N*-Dimethylformamide (DMF) was obtained from Sinopharm Chemical Reagent Co., Ltd. Calcium chloride dihydrate, sodium chloride, magnesium chloride hexahydrate, and calcium nitrate tetrahydrate were purchased from Sinopharm Chemical Reagent Co., Ltd. PEOZ with an average molecular weight of ~10 400 was synthesized by cationic ring-opening polymerization according to Hoogenboom *et al.*[44] Dimethyl sulfoxide-d_6 (DMSO-d_6, D.99.9% + 0.03% TMS) was purchased from Macklin Inc., China.

Sample preparation

The hybrids of PEOZ and PHS were made *via* solution blending in DMF at a concentration of 15 wt%. The hybrid films were cast on a PTFE mold at room temperature for 48 h to evaporate DMF and dried in a vacuum oven at 60 °C for 48 h. In order to prepare samples containing soluble salts, $CaCl_2 \cdot 2H_2O$, for example, was dissolved in DMF and then added in the polymer hybrid (30PHS/PEOZ) in the DMF solution at different molar ratios of metal ion to the active group. After stirring for 24 h, the solution was ready for making film specimens and for chemical analysis.

Characterization methods

Optical images of the self-healing process of each sample were captured using an Olympus BX51 microscope under visible light. The three dimensional (3D) morphology of the scratches in the self-healing tests was measured using a Leica SP8 confocal laser scanning microscope with an excitation laser of 488 nm, scanning area 1.55 mm × 1.55 mm. Micro-Fourier Transform Infrared (micro-FTIR) mapping was carried out by using a Thermo Nicolet Scientific iN10 infrared imaging microscope. Ultraviolet-Visible (UV-Vis) spectroscopy titration experiments were implemented using a Perkin Elmer Lambda 35 UV-Vis spectrometer. The spectra were recorded 2 min after mixing the salt with the polymers in DMF. The spectra were re-recorded after five minutes to ensure the accuracy of the results. The infrared spectra of the samples were recorded through 32 scans on each sample using a Thermo Scientific Nicolet iS50 FT-IR spectrometer with the ATR module in the range of 650–4000 cm^{-1}. Solid state ^{13}C Nuclear Magnetic Resonance (NMR) and liquid state ^{1}H NMR measurements were carried out using a Bruker AVANCE III 400 spectrometer. X-ray Photoelectron Spectroscopy (XPS) spectra were recorded on a Shimadzu/Kratos

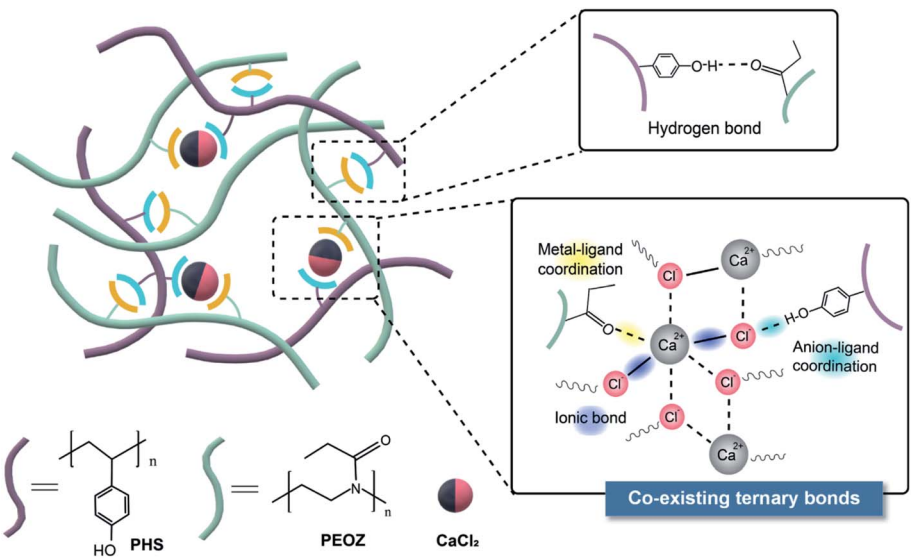

Scheme 1 Schematic diagram of the self-healing structure composed of the hydrogen bonds, metal–ligand coordination, and ionic bonds.

Axis Supra spectrometer. All spectra were calibrated to the neutral carbon peak at 284.8 eV.

An Instron 5942 tensile testing machine equipped with a 500 N load cell was used to perform the mechanical strength test, in which the dumbbell-like type 5B samples were cut from the films according to ISO 527, and the gauge length was 10 mm. The test speed was set at 2.5 mm min^{-1}, and Young's modulus was derived from the curve in the elongation range of 0.05% to 0.25%. In the single-lap tensile shear strength test, the sizes of the specimens were: 50 × 12 mm^2 (aluminum), 61 × 18 mm^2 (plywood), 76 × 25 mm^2 (glass), and the bonded area sizes were 12 × 6 mm^2 (aluminum), 18 × 8 mm^2 (plywood), 25 × 8 mm^2 (glass). The specimens were left to cure for 3 days before the test, and the thickness of the adhesive layer was about 100 μm. The test speed was 5 mm min^{-1}. All the mechanical tests were replicated at least five times.

Molecular dynamics simulations

Molecular Dynamics (MD) simulation was utilized to calculate the interaction energy and to simulate the self-healing process of the 30PHS/PEOZ hybrid. Materials Studio 7.0 (Accelrys, USA) was employed to establish the initial model with PEOZ and PHS molecular chains. The model of the 30PHS/PEOZ consisted of eight chains of PEOZ and three chains of PHS. There were 105 repeat units in each chain of PEOZ with a molecular weight of about 10 400 and 92 repeat units in each chain of PHS with a molecular weight of approximately 11 000. PEOZ/PHS/$CaCl_2$ under dry conditions was developed by adding 390 molecules of crystal H_2O, 195 Ca^{2+} ions, and 390 Cl^- ions into the PEOZ/PHS system. And 147 molecules of H_2O were respectively added into the two hybrid systems in order to further simulate the wet condition according to the water vapor absorption experiment. The size of the initial computational cells was 300 Å × 300 Å × 300 Å with the 3D periodic boundary condition. GROningen MOlecular Simulation (GROMOS) force field version 54A7 (ref. 45) was adopted to characterize the atomic interactions in the PEOZ/PHS/$CaCl_2$ system. GROningen MAchine for Chemical Simulation (GROMACS)[46] was used to carry out the molecular simulations of the self-healing. The force field parameters of PEOZ and PHS residues were obtained on the Automated Topology Builder (ATB) platform.[47]

After establishing the initial configuration, energy minimization, equilibrium, and dynamic simulation were performed in this order. The optimal system was when the forces reached the reset tolerance of 10 kJ mol^{-1} nm^{-1}, or minimization steps were performed up to the maximum number of iteration steps that were set at 20 000. After energy minimization, the configuration was later equilibrated under the *NVT* ensemble (constant number of particles (*N*), volume (*V*), and temperature (*T*)). The total simulation time was 1 ns with a 1 fs time step at 1 atm and 300 K. To simulate the real temperature rising, annealing simulations were used under the *NVT* ensemble. The computational cells were about 60 Å × 60 Å × 60 Å, and the density of the system was 1.08 g cm^{-3}, which was close to the densities of the as-received PEOZ and PHS (1.14 g cm^{-3} and 1.16 g cm^{-3}, respectively).

The self-healing of the hybrid was determined by setting the periodic boundary condition in the *x*–*y* direction. *NVT* and *NPT* (constant number of particles (*N*), pressure (*P*), and temperature (*T*)) equilibrations were repeated to obtain an appropriate and steady molecular configuration as another procedure of sequential energy minimization. A copy of the cell was created close to the first to form a layered artificial crack of 10 Å representing the self-healing interface.[48] The process of self-healing was simulated using the equilibrium MD simulation for 2 ns. MSD is defined as:

$$\mathrm{MSD} = \langle |r_i(t) - r_i(0)|^2 \rangle \quad (1)$$

where $\langle\ \rangle$ refers to the average of all atoms, $r_i(t)$ is the position vector of atom i at time *t* and $r_i(0)$ is the position vector of atom i at the initial time. Finally, a non-equilibrium pulling simulation was carried out for 2 ns to evaluate the bonding strength of the self-healing interface.

Results and discussion

Self-healing of PHS/PEOZ and the effect of $CaCl_2$ on the self-healing property

In order to optimize the amount of PHS, a series of blend materials were prepared at a PHS/PEOZ weight ratio of 0 : 100, 15 : 85, 30 : 70, 50 : 50, 70 : 30, and 100 : 0 (labeled PEOZ, 15PHS/PEOZ, 30PHS/PEOZ, 50PHS/PEOZ, 70PHS/PEOZ, and PHS, respectively). DSC and FTIR were adopted to characterize the hybrid materials (Fig. S1 and Table S1†). The results suggest that the hybrids of PEOZ and PHS have good miscibility due to the hydrogen bonding between PEOZ and PHS.

Then the films of the hybrids cast on glass slides were scratched with an approximately 30 μm wide cut by a scalpel blade. The self-healing process of the films was observed when the samples were placed in a humidity chamber at 95% relative humidity (RH). The 15PHS/PEOZ film heals the fastest among the hybrids (within 50 min) (Fig. S2a†), and the cut of 30PHS/PEOZ heals gradually within 70 min (Fig. S2b†). In contrast, the 50PHS/PEOZ and 70PHS/PEOZ films do not have self-healing ability (Fig. S2c and S2d,† respectively). The self-healing systems generally have a mobile phase around the damaged area.[49] Based on the DSC measurements recorded in Fig. S1a,† the increase of PHS enhances T_g, indicating lower polymer chain mobility, which thereby results in longer healing time. On the other hand, it is found that the addition of PHS decreases the moisture uptake (Fig. S3a†), which shows the same trend with the self-healing speed. Therefore, it is obvious that water contributes to triggering the self-healing process, similar to the reports that water increases the chain mobility of the polymers as the plasticizer for self-healing.[9,50–52] Additionally, under the same dew point, when the temperature is raised (RH will decrease relatively), the healing rate is much slower (Fig. S4†), indicating that the relative humidity is more crucial than the dew point.

The 30PHS/PEOZ sample was selected to perform further investigation of the self-healing properties because it exhibits excellent self-healing ability and good adhesion in a humid

environment at the same time (Fig. S3b†). $CaCl_2$ was mixed with the polymer hybrid at different molar ratios (Ca^{2+}: carbonyl groups of PEOZ equals 1 : 6, 1 : 4, 1 : 2, 1 : 1, and 2 : 1). After the evaporation of the solvent, the cured films with more than 0.5 equivalent of $CaCl_2$ (Ca^{2+} : C═O of 1 : 2) illustrate the salt efflorescence (Fig. S5†). The crystallization of $CaCl_2$ appears obviously, which affects the optical properties and further application of the films. Therefore, Ca^{2+} : C═O molar ratios of 1 : 6 and 1 : 4 were respectively selected in the self-healing experiments. A confocal laser scanning microscope was employed to measure the width and depth of each scratch. There is no significant difference in the healing rate when 0.17 equivalent of $CaCl_2$ is added (Fig. 1b). By comparison, the self-healing is accelerated with the addition of 0.25 equivalent of $CaCl_2$, and the scratch heals within 60 min (Fig. 1c), faster than the neat 30PHS/PEOZ (Fig. 1a) even taking into consideration the larger scratch.

The self-healing efficiency of the hybrids

The mechanical strength of the healed sample was measured through tensile and adhesion strength tests to evaluate the efficiency of the self-healing process. In the tensile strength test, each sample was cut with scissors into two parts, which were put together with an approximately 1 mm overlap on a polytetrafluoroethylene (PTFE) board (Fig. 2a).[12] Together with the original samples, the reconnected samples were placed into a humidity chamber for 5 h to completely self-heal the samples and ensure that all samples have experienced the same environment. The calculation of the stress was based on the single thickness of the specimens instead of the double thickness because most of the specimens broke outside the overlapped area. Fig. 2b and c show the tensile–strain curves, and the data are summarized in Table 1. Here, the healing efficiency is defined as the ratio of the tensile strength of the healed sample to that of the original sample. For the 30PHS/PEOZ samples, the healing efficiency is 82% and increases to 91% for the samples containing $CaCl_2$ after the same healing time. It is remarkable that Young's modulus of the sample containing $CaCl_2$ is ≥40% higher than that of 30PHS/PEOZ for both original and healed samples. The tensile strength is also increased by nearly 14% for the healed samples. The enhancement of Young's modulus and healing efficiency can be attributed to the increasing interactions in the system containing $CaCl_2$, as well as the simultaneous functions yielded by the bond rupture–reformation and the internal friction of the ionic bonds[53] of $CaCl_2$. These findings indicate that $CaCl_2$ strengthens the 30PHS/PEOZ film and promotes self-healing efficiency to a certain extent.

The self-healing property permits 30PHS/PEOZ to be used as a repeatable adhesive. Fig. 2d shows the schematic procedures of the single-lap tensile shear test. After the two halves of the specimens were pulled to failure, they were quickly adhered to each other again with a force of about 50 N (removed after 30 min) and stored in the humidity chamber at RH ≈ 95% for 5 h. The debonding–rebonding procedures were repeated two times, and the healing efficiency was calculated as the ratio of the re-bonded adhesion strength to the original one. Fig. 2e and f show the curves of the adhesion strength against the displacement, and the data are listed in Table 2. The results show that the 30PHS/PEOZ samples containing $CaCl_2$ demonstrate higher healing efficiencies, and the adhesion strength is also stronger than the neat 30PHS/PEOZ at RH ≈ 95%. In addition, 30PHS/PEOZ can repeatedly adhere under ambient conditions (RH ≈

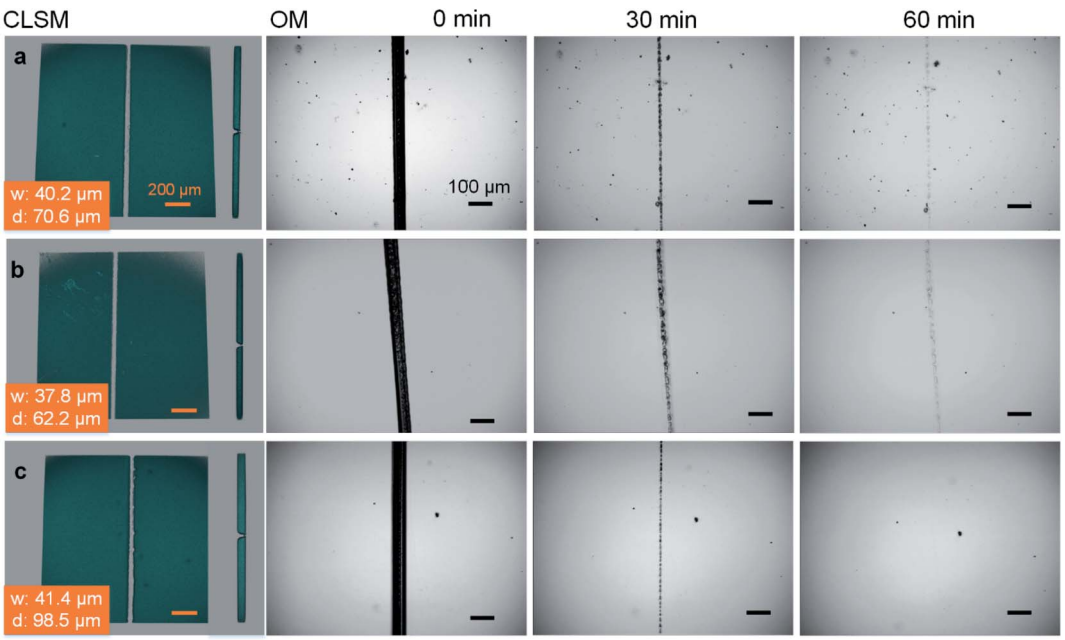

Fig. 1 Self-healing of 30PHS/PEOZ with $CaCl_2$. 3D laser microscopic images and optical photographs of the self-healing process of (a) 30PHS/PEOZ, 30PHS/PEOZ with (b) 0.17 equivalent $CaCl_2$ and (c) 0.25 equivalent of $CaCl_2$. The healing rate of 30PHS/PEOZ was improved by the addition of 0.25 equivalent of $CaCl_2$. CLSM: confocal laser scanning microscope, OM: optical microscope, *w*: width, *d*: depth.

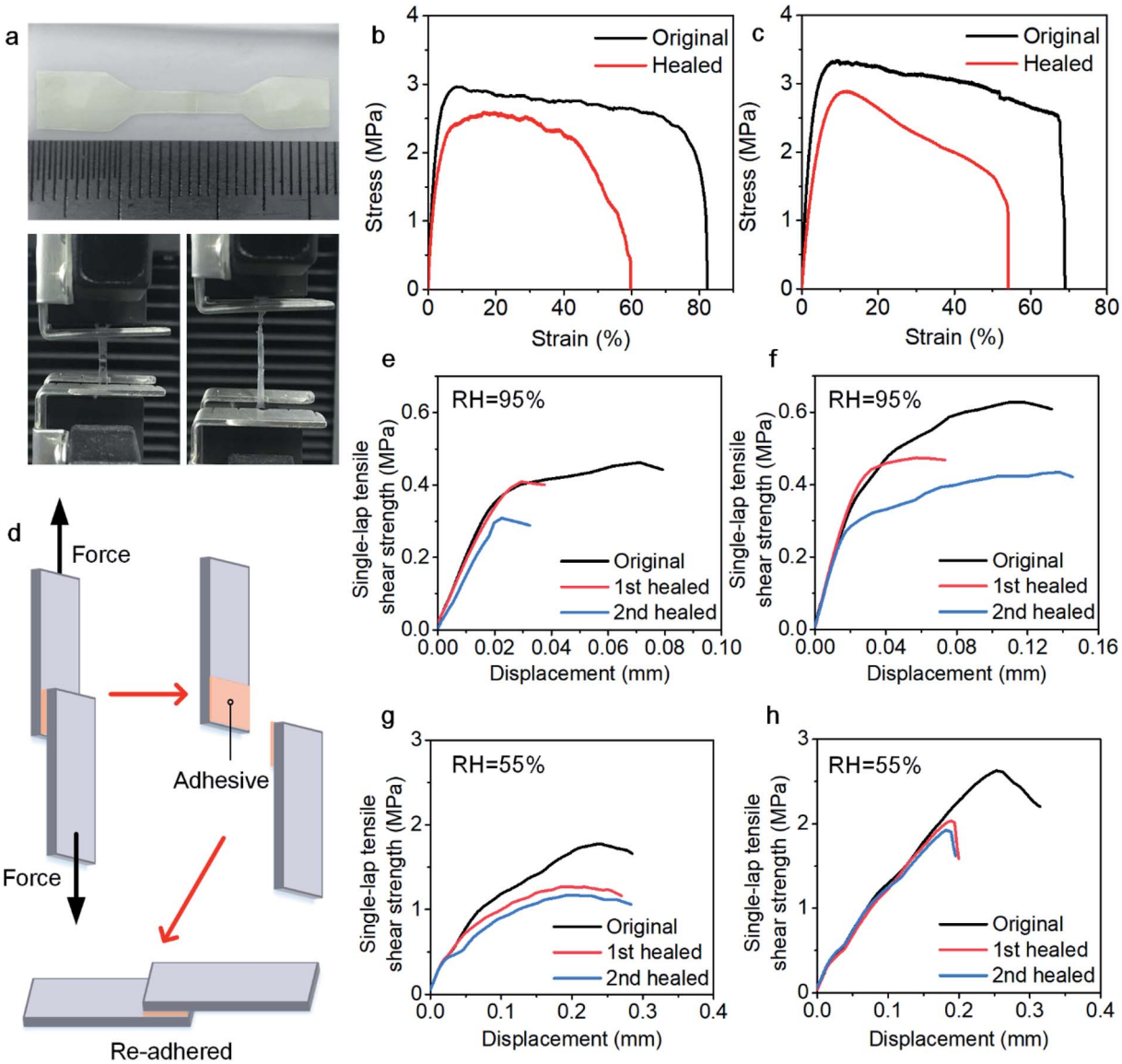

Fig. 2 Self-healing efficiency test. (a) Samples were cut and overlapped ~1 mm at RH ≈ 95% for 5 h, and the tensile tests were carried out in an ambient environment. The tensile stress–strain curve of (b) 30PHS/PEOZ and (c) 30PHS/PEOZ + $CaCl_2$ at RH ≈ 95%. (d) Scheme of the single-lap tensile shear strength test and repeatable adhesion. The repeatable adhesion strength of (e) 30PHS/PEOZ at RH ≈ 95%, (f) 30PHS/PEOZ + $CaCl_2$ at RH ≈ 95%, and (g) 30PHS/PEOZ at RH ≈ 55%, (h) 30PHS/PEOZ + $CaCl_2$ at RH ≈ 55%.

Table 1 Summary of the mechanical properties of the 30PHS/PEOZ hybrids with/without $CaCl_2$

	Tensile strength (MPa)			Elongation at break (%)		Young's modulus (MPa)	
Sample	Original	Healed	Healing efficiency	Original	Healed	Original	Healed
30PHS/PEOZ	3.03 ± 0.22	2.49 ± 0.08	82.26%	80.59 ±5.92	59.89 ± 6.61	99.16 ±7.63	90.81 ± 5.87
+ $CaCl_2$	3.11 ± 0.36	2.83 ± 0.15	91.23%	62.03 ± 7.16	41.64 ± 7.35	138.52 ±14.10	133.75 ± 4.56

55%) as well (Fig. 2g and h). It is noted that because absorbed water works as a plasticizer, the adhesion strength of both neat 30PHS/PEOZ and hybrids containing $CaCl_2$ is higher than that in the wet environment (RH ≈ 95%), however, the self-healing efficiency in moderate humidity is slightly lower. In conclusion, $CaCl_2$ is proved to enhance the adhesion strength and the healing efficiency of 30PHS/PEOZ in both wet and ambient environments.

Self-healing mechanisms

FTIR spectra have shown that PEOZ and PHS are connected *via* hydrogen bonding (Fig. S1†). Since water vapor would weaken

Table 2 The adhesion strength and the healing efficiency of the 30PHS/PEOZ hybrids with/without $CaCl_2$ under different relative humidities

	RH ≈ 95%		RH ≈ 55%	
Healing efficiency	30PHS/PEOZ	+ $CaCl_2$	30PHS/PEOZ	+ $CaCl_2$
Original adhesion (MPa)	0.44 ± 0.03	0.64 ± 0.06	1.80 ± 0.04	2.57 ±0.09
First healed	72.15 ± 4.76%	81.36 ± 3.06%	69.14 ± 5.22%	74.06 ± 3.39%
Second healed	61.28 ± 3.29%	70.31 ± 5.60%	59.36 ± 2.51%	65.83 ± 5.81%

the hydrogen bonds between the two polymers,[50] micro-FTIR mapping was adopted to monitor whether PEOZ and PHS move simultaneously. The peak at 1624 cm^{-1} is the C═O stretching band of PEOZ, and 1509 cm^{-1} is the semicircle stretching modes of the benzene in PHS.[54] These two peaks are used as the characteristic peaks for the two components. Fig. 3a shows that during the self-healing process of 30PHS/PEOZ, the intensities of both peaks gradually increase in the scratched area, which indicates that PHS and PEOZ move to the edges of the scratch at a similar pace and contact the other side of the scratch gradually. After 70 min, the intensity distribution of the two characteristic peaks is relatively homogeneous, which implies the end of the self-healing process. It also proves that moisture does not destroy the interaction between PEOZ and PHS. Fig. 3b shows that the addition of $CaCl_2$ does not affect the synchronization and, instead, accelerates the self-healing process to finish within 60 min. This acceleration mechanism by $CaCl_2$ was further evaluated through simulations and experiments in the following sections.

The chemical interactions were studied by Molecular Dynamics simulations. To simplify the calculations, PEOZ of lower average molecular weight (~10 400) was used in the simulation system, which also has the self-healing capability, as shown in Fig. S6.† Fig. 3c shows the model of 30PHS/PEOZ and 30PHS/PEOZ + $CaCl_2 \cdot 2H_2O$. The average interaction energies between PEOZ, PHS, and ions (cations or anions) of $CaCl_2$ in both dry and wet environments are recorded in Fig. 3d. Interestingly, Ca^{2+} and Cl^- exhibit selective interaction with PEOZ and PHS, respectively. Ca^{2+} shows higher interaction energy with PEOZ, whilst Cl^- has greater interaction energy with PHS, indicating that PEOZ strongly pairs with Ca^{2+} ions, while PHS prefers to bond to Cl^- ions. Additionally, the interaction energy between Ca^{2+} and Cl^- in the hybrid system is calculated as -7.92×10^5 kJ mol^{-1} owing to the strong ionic bonding of $CaCl_2$. A bridging interaction is established to connect the 30PHS/PEOZ + $CaCl_2$ hybrid system as: PEOZ ← Ca^{2+} ↔ Cl^- → PHS. Moreover, this preferential interaction trend is not affected by adding environmental water molecules into the system, which simulates the experimental parameter.

The self-healing process at the molecular scale has also been simulated by creating a cell with an artificial crack of 1 nm (Fig. 3e). The motions of the cells during self-healing can be characterized by the mean square displacement (MSD) at a particular simulation time. Fig. 3f shows the curves of MSD against the simulation time of 30PHS/PEOZ and 30PHS/PEOZ + $CaCl_2$, and the diffusion coefficient D of each system can be deduced from the increment of MSD with time according to the simplified equation:

$$D = \frac{a}{6} \quad (2)$$

where a is the slope of the straight line fitted from the MSD curve.[48] The diffusion coefficient of 30PHS/PEOZ is 1.717×10^{-6} cm^2 s^{-1}, while the $CaCl_2$ containing system has a higher diffusion coefficient of 2.117×10^{-6} cm^2 s^{-1}, which agrees with the experimental results showing faster self-healing with the addition of $CaCl_2$ (Fig. 1c). On the other hand, the potential of mean force needed to separate the self-healed system containing $CaCl_2$ is nearly four times stronger than that of the neat 30PHS/PEOZ (Fig. 3g), indicating stronger bonding strength of 30PHS/PEOZ + $CaCl_2$, which is consistent with the experimental results (Fig. 2).

These preferential interactions among PEOZ, PHS, and $CaCl_2$ suggested by the MD simulations were experimentally validated using spectral analysis. First of all, we used Raman spectroscopy to confirm the existence of bonding between Ca^{2+} and Cl^- in 30PHS/PEOZ + $CaCl_2$ in both ambient and wet environments (Fig. S7†). In the UV-Vis absorption titration experiments, the n–π* electronic transition of PEOZ at 268 nm gradually red-shifts and becomes broader upon the addition of $CaCl_2$ to PEOZ. Meanwhile, a new absorption at 289 nm is generated and increases with the increasing ratio of Ca^{2+} (Fig. 4a). In contrast, the π–π* absorption peak of PHS[55] does not change, and no new peak is generated when different amounts of $CaCl_2$ are added (Fig. S8a†). In the FTIR study, as shown in Fig. 4b, the C═O band at 1624 cm^{-1} of PEOZ shifts to 1606 cm^{-1} for the films containing $CaCl_2$, and the O═C–N amide stretching band at 1472 cm^{-1} (ref. 56) moves to the higher wavenumber at 1486 cm^{-1}. The result indicates that Ca^{2+} coordinates with the oxygen in the carbonyl group of PEOZ, but not with nitrogen, consistent with the coordination between tertiary amide and metals.[57] On the other hand, no shift of the C–O band around 1230 cm^{-1} of PHS is observed when $CaCl_2$ is added into PHS (Fig. S8b†), implying that Ca^{2+} does not coordinate with PHS.[32] Besides, XPS reveals that the Ca $2p_{1/2}$ and Ca $2p_{3/2}$ peaks of $CaCl_2$ at 351.6 eV and 348.1 eV shift to 351.2 eV and 347.8 eV respectively after being blended with 30PHS/PEOZ (Fig. 4c), further confirming the coordination between Ca^{2+} and PEOZ. Since the hydroxyl band of PHS in the IR spectra is heavily affected by the environment humidity and the existing hydrogen bonds between PHS and PEOZ, it becomes hard to evaluate the variation of the hydrogen bonding by using the FTIR spectroscopy. Therefore, the interaction between PHS and

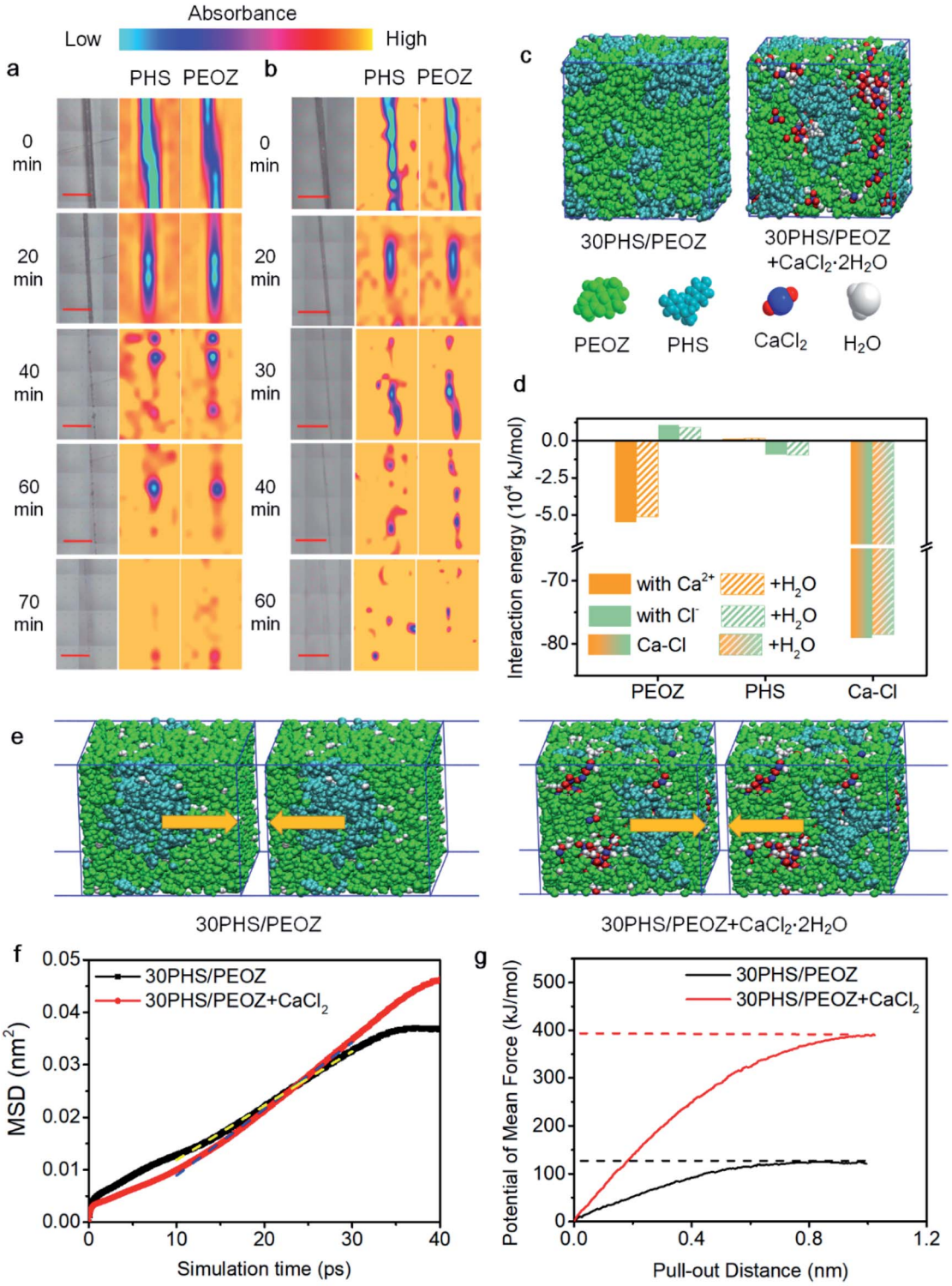

13

Fig. 3 Spectral mapping and the simulations of the self-healing process of 30PHS/PEOZ with $CaCl_2$. The self-healing monitoring by micro-FTIR mapping analysis on the surface of (a) 30PHS/PEOZ and (b) 30PHS/PEOZ + $CaCl_2$. The optical images display the scratched area of the films. The false-color mapping images, of which the peak at 1509 cm^{-1} refers to PHS, and the peak at 1624 cm^{-1} is assigned to PEOZ, indicate the distribution of PHS and PEOZ respectively during the self-healing process (scale bars: 100 μm). (c) The computational cells of the 30PHS/PEOZ and 30PHS/PEOZ + $CaCl_2$. (d) The interaction energy of PEOZ and PHS with Ca^{2+} and Cl^-, and the interaction energy between Ca^{2+} and Cl^-, respectively, "+H_2O" means wet condition. (e) The equilibrated configuration for the wet environment self-healing simulation. (f) Mean square displacement *vs.* simulation time of 30PHS/PEOZ and 30PHS/PEOZ + $CaCl_2$. (g) The curves of the potential of mean force against the pull-out distance after self-healing.

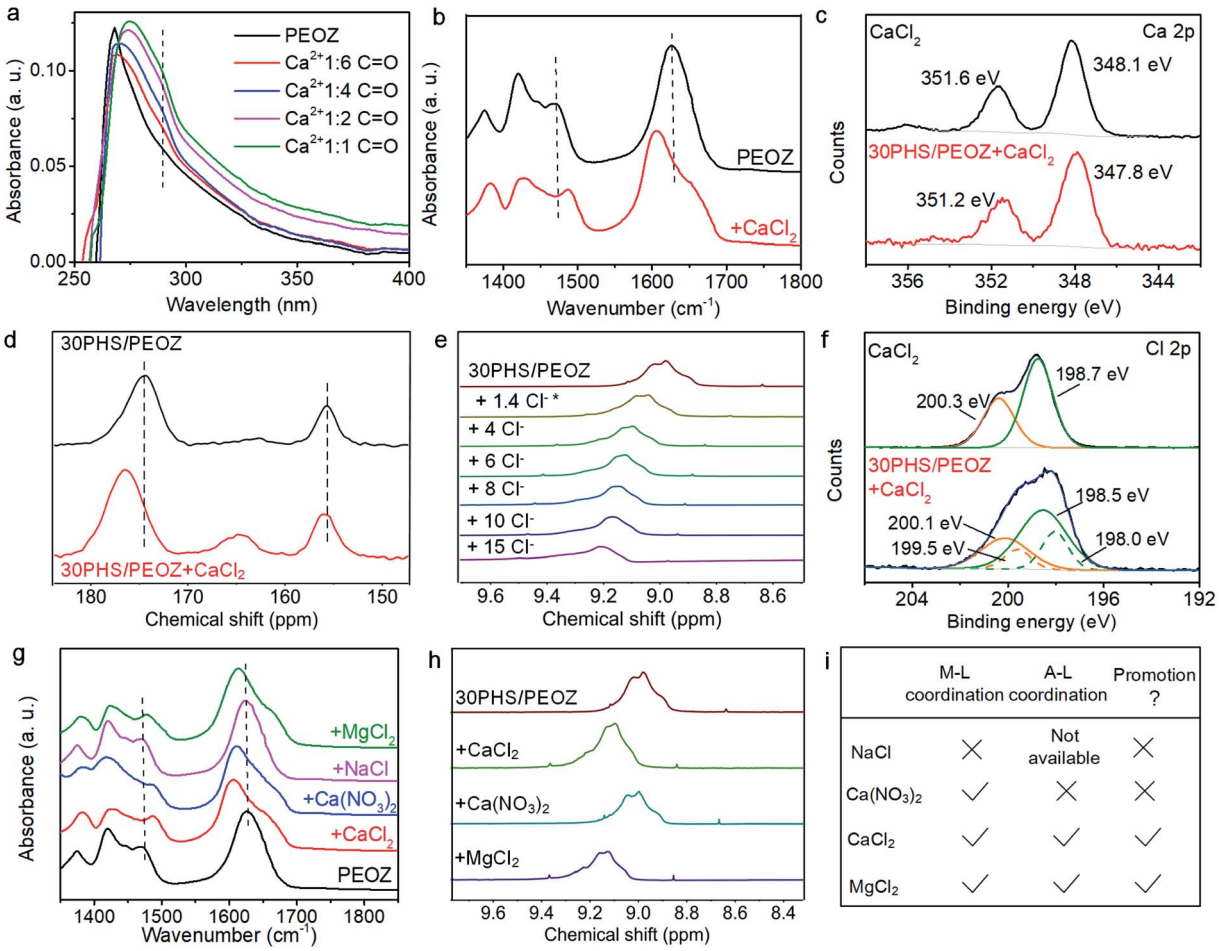

Fig. 4 (a) UV-Vis spectra of PEOZ in the titration experiment with the addition of $CaCl_2$ in DMF. (b) The carbonyl group red-shifts, and the amide C–N bond blue-shifts in the FTIR spectra of PEOZ because of the coordination with Ca^{2+}. (c) XPS spectra of deconvolution of Ca 2p peaks for pristine $CaCl_2$ and 30PHS/PEOZ + $CaCl_2$. (d) The ^{13}C NMR resonance signals of the carbonyl carbon of PEOZ and hydroxyl-substituted carbon of PHS. (e) Partial ^1H NMR spectra of 30PHS/PEOZ in DMSO-d_6, the –OH signal moves downfield with an increasing ratio of $CaCl_2$. The ratio of Cl^- at 1.4 equiv. is the ratio used in the self-healing experiment. (f) XPS spectra of the deconvolution of Cl 2p peaks for pristine $CaCl_2$ and 30PHS/PEOZ + $CaCl_2$, the solid line and dashed line refer to the two different deconvolutions of Cl 2p doublets, respectively. (g) Partial FTIR spectra of PEOZ and the samples containing $CaCl_2$, $Ca(NO_3)_2$, NaCl, and $MgCl_2$. (h) Partial ^1H NMR spectra of 30PHS/PEOZ in DMSO-d_6, with the 1 equivalent addition of $CaCl_2$, $Ca(NO_3)_2$, and $MgCl_2$. (i) Comparison of the interactions between the polymers and different salts, and whether the self-healing is promoted. M–L: metal–ligand, A–L: anion–ligand. The anion–ligand coordination result of NaCl is not available because NaCl is not soluble in DMSO, and thus the spectrum is not present.

$CaCl_2$ was examined using NMR and XPS measurements. The solid state ^{13}C NMR spectra show that the introduction of $CaCl_2$ causes a slight downfield shift of the peak from 155.8 ppm to 156.2 ppm, which corresponds to the hydroxyl-substituted carbon (C–OH) of PHS (Fig. 4d and S9†). This can be attributed to the change of the hydrogen bonding acting on C–OH.[58] In addition, comparing the C=O signal of PEOZ at 174.4 ppm in 30PHS/PEOZ *versus* that in 30PHS/PEOZ + $CaCl_2$, this peak undergoes a strong downfield shift of $\Delta\delta = 2.8$ ppm in 30PHS/PEOZ + $CaCl_2$ due to the metal–ligand coordination.[59] Liquid state ^1H NMR spectra are obtained to further investigate the status of the hydroxyl of PHS by the titration experiment of $CaCl_2$ into 30PHS/PEOZ in DMSO-d_6 (Fig. S10†). Fig. 4e shows the change of the chemical shift position of the O–H proton in PHS. It is clear that the peak shifts downfield gradually with the addition of $CaCl_2$, implying the formation of a hydrogen bond.[60] In the XPS measurements, Fig. 4f shows that the doublet Cl $2p_{1/2}$ and Cl $2p_{3/2}$ peaks become indistinguishable in 30PHS/PEOZ + $CaCl_2$ when compared with the pristine $CaCl_2$. The spectrum can be deconvoluted into two sets of Cl 2p doublets, which implies that the chemical state of chlorine has changed. Ebner *et al.* have reported that the resolution loss of Cl 2p peak is due to the presence of hydrogen bonding and different types of chlorine environments.[61] Additionally, chloride anion shows fine affinity for phenolic compounds as a hydrogen bond acceptor.[62] Thus, it is reasonable to conclude that Cl^- forms hydrogen bonds with the hydroxyl group of PHS, confirming the MD simulation results.

In summary, the self-healing mechanism of PHS/PEOZ can be described as follows. When the hybrid film is damaged, the intermolecular hydrogen bonds are more likely to break than the covalent bonds of the polymers. At first, the film absorbs

water from the environment, which enables the system to form a mobile phase. When the space between the fractured surfaces is sufficiently narrow, the hydrogen bonds will regenerate between PEOZ and PHS. Furthermore, the promoted self-healing process of the $CaCl_2$ containing hybrid system is achieved by the co-existing ternary bridging bonds: hydrogen bonding, metal–ligand coordination, and ionic bonding. In this system, $CaCl_2$ acts as the connector between PEOZ and PHS. This mechanism is different from the reported common metal–ligand coordination self-healing mechanisms because both cation and anion contribute to this system. Ca^{2+} mainly coordinates with the carbonyl groups of PEOZ, while Cl^- forms hydrogen bonds with the hydroxyl groups of PHS. Upon absorbing moisture, the coulombic interaction between Ca^{2+} and Cl^- accelerates the chains of PEOZ and PHS to diffuse toward the interface of the fracture,[63] which promotes the healing rate. The use of $CaCl_2$ in the self-healing films was previously reported in conjunction with byssus protein hydrolysate[64] and catechol polymer;[32] however, it was considered that only Ca^{2+} forms complexes with the polymer and facilitates self-healing behavior. In this work, we have evidenced that the Cl^- anion also plays a vital role in the self-healing process, empowering the anion coordination to the design and function of self-healable structures. The role of the ternary bonds in enhancing the mechanics of the material is also evaluated by comparison of the tensile behavior of each component (Fig. S11†).

Moreover, in order to validate this mechanism, $MgCl_2$, NaCl, and $Ca(NO_3)_2$ salts were separately added into 30PHS/PEOZ, and the self-healing rates were compared (Fig. S12†). The sample with $MgCl_2$ shows a comparative healing rate with the sample containing $CaCl_2$, while the samples containing NaCl or

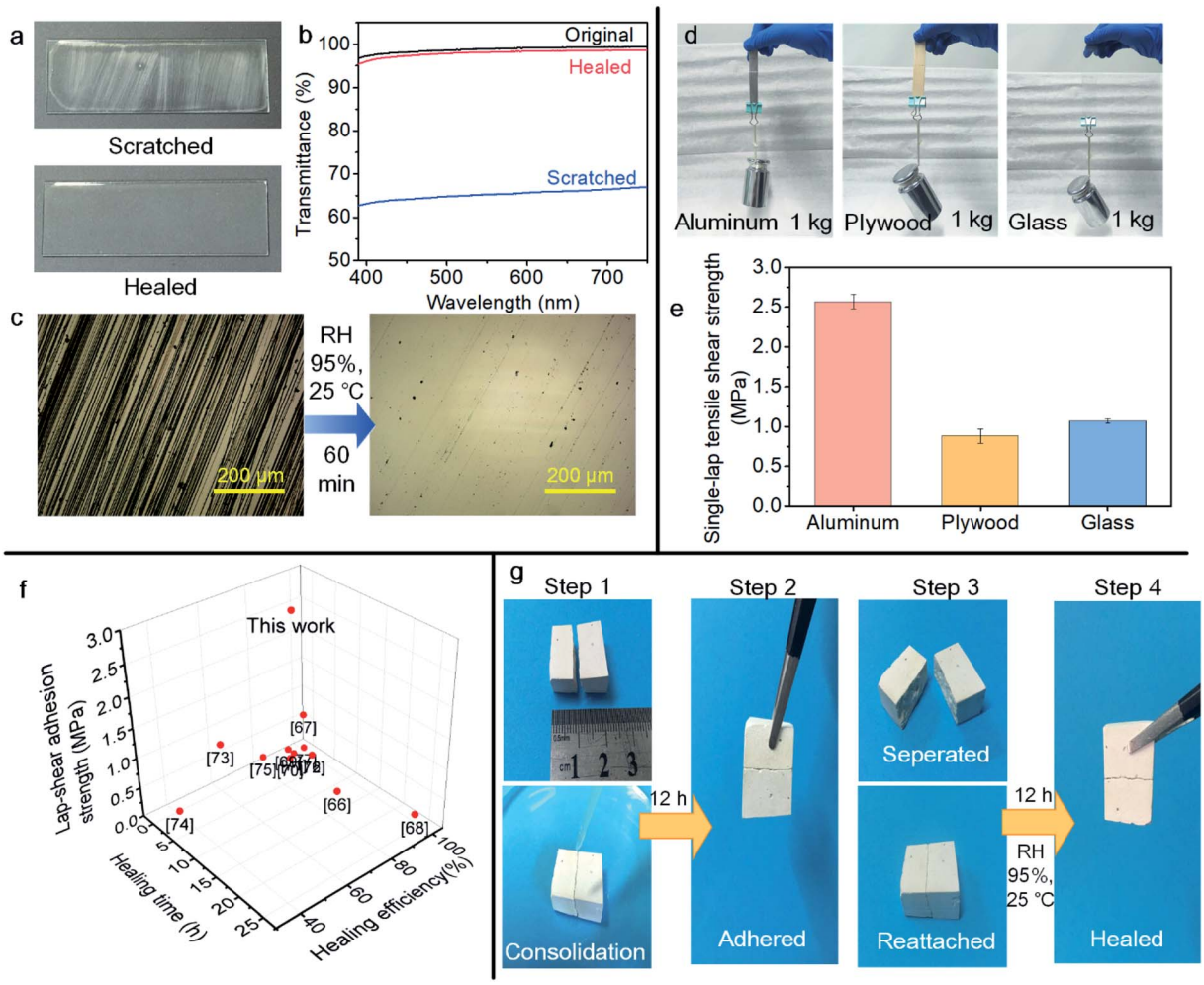

Fig. 5 Applications of the 30PHS/PEOZ + $CaCl_2$ hybrid. (a) The photographs of sandpaper-scratched 30PHS/PEOZ + $CaCl_2$ film and self-healed film in 95% RH chamber for 60 min. (b) The recovery of the transmittance of visible light after self-healing recorded in UV-Vis spectra. (c) Optical images of the scratched surface and the healed surface of the 30PHS/PEOZ + $CaCl_2$ film. (d) Adhesion and (e) the single-lap tensile shear strength of the 30PHS/PEOZ + $CaCl_2$ on different substrates. (f) Comparison of healing time and healing efficiency *versus* adhesion strength of 30PHS/PEOZ + $CaCl_2$ with the self-healable adhesives reported in the recent three years.[66–77] (g) The self-healing of a consolidated plaster fragment. Step 1: the fragment was pre-treated with $CaCl_2$ solution and split into two parts, and the two halves were joined together. 1.2 mL 30PHS/PEOZ in DMF at a concentration of 15% was dropped on the sample. Step 2: the sample was cured for 12 h. Step 3: the sample was separated and reattached. Step 4: the adhesion of the fragmented sample was restored after being put in a wet environment for another 12 h.

$Ca(NO_3)_2$ did not improve the healing rate. As shown in Fig. 4g, for the films containing $Ca(NO_3)_2$ and $MgCl_2$, the C=O band and the C–N amide stretching band of PEOZ move as the $CaCl_2$ containing sample does, whereas these two characteristic bands remain stable for the film with NaCl, indicating that PEOZ prefers to coordinate with Ca^{2+} and Mg^{2+} rather than Na^+. Fig. 4h and S13† show the ^1H NMR spectra of the samples, it is clear that with the addition of $CaCl_2$ and $MgCl_2$, the O–H peaks move downfield, whereas, $Ca(NO_3)_2$ does not affect the position of the O–H signal. These supplementarily confirm that Cl^- forms hydrogen bonding with PHS, and the hydrogen bonding between NO_3^- and –OH of PHS is rather weak. $MgCl_2$ shares similar coordination behavior with $CaCl_2$, while neither NaCl nor $Ca(NO_3)_2$ connects the two polymers. Therefore, whether the cation and anion of the added salt respectively interact with the polymers to form the ternary bonds in the hybrid is the key finding of the self-healing mechanism (Fig. 4i).

Applications of 30PHS/PEOZ with $CaCl_2$

The 30PHS/PEOZ + $CaCl_2$ film shows excellent visible light transmittance. At a thickness of the cast film of about 50 μm, the transmittance is higher than 95% over the wavelength from 380 to 750 nm (T_{550} = 98.9%), which indicates that the use of the hybrid as an adhesive or a coating brings minimum aesthetic effects on the adhered surface. Fig. 5a demonstrates that the film becomes obscure after being scratched by sandpaper, and the light transmittance visibly decreases (Fig. 5b). Interestingly, the light transmission of the film can be effectively restored in the humid environment within 60 minutes due to the excellent self-healing property of the 30PHS/PEOZ + $CaCl_2$ hybrid (Fig. 5b and c).

In addition, most of the self-healable adhesives nowadays are hydrogels,[49] but their physical properties and low adhesion strength hinder their broader applications. Here, the 30PHS/PEOZ + $CaCl_2$ hybrid displays good adhesion on impermeable and porous surfaces. For example, the 30PHS/PEOZ + $CaCl_2$ solution was used to bind two slices (each) of aluminum, plywood, and glass, and all the samples are able to bear a load of 1 kg (Fig. 5d). The adhesion strength on aluminum, plywood, and glass is 2.57 ± 0.09 MPa, 0.88 ± 0.08 MPa, and 1.07 ± 0.03 MPa, respectively (Fig. 5e), which leads to a promising application of 30PHS/PEOZ + $CaCl_2$ as a self-healable transparent adhesive material. Additionally, the 30PHS/PEOZ + $CaCl_2$ hybrid shows outstanding performance compared with the most recently published room temperature self-healing coatings and hydrogels taking into consideration transparency, adhesion strength, and self-healing conditions (Fig. 5f and Table S2†).

Nowadays, the majority of the conservation materials are polymeric materials, and they often function as adhesives, consolidants, and protective coatings. However, not only the cultural heritage but also the conservation materials suffer from degradation, especially from mechanical damage, resulting in micro-cracks on the materials. The damaged conservation materials are generally difficult to be cleaned and replaced by new materials.[65] Novel materials with healing properties for the conservation of cultural heritage are more desirable. As an example of potential applications, the 30PHS/PEOZ hybrid has been used for the preservation of cultural heritage by taking advantage of self-contained water-soluble salts in the ancient supporting layer of wall paintings (for the elemental contents, refer Table S3 in the ESI†). More importantly, the onsite conservation environment of wall paintings usually has high relative humidity. Here, a simulating consolidation treatment was carried out on a fragment of plaster. Before the test, the fragment absorbed a $CaCl_2$ solution of 10 mg mL^{-1} by capillary absorption and was split into two parts. Fig. 5g shows the treatment of the broken fragments with the hybrid, and the fragments were left curing for 12 h in order to completely recombine the two halves (Step 1 and Step 2). Then the fragment was separated by breaking the adhesion at the interface. Next, the fragments were tightly reattached together and placed in the humidity chamber (RH ≈ 95%) for 12 h (Step 3). The SEM images (Fig. S14†) suggest that the porous organic film adhered to the fracture of the sample, demonstrating one exemplary application of self-healing materials in the field of conservation of cultural heritage.

Conclusions

A multifunctional self-healing material of the PEOZ, PHS, and $CaCl_2$ hybrid has been developed and can be used as a strong transparent adhesive in both ambient and wet environments (RH ≈ 95%), demonstrating excellent self-healing capability and repeatable adhesion. A new mechanism of the self-healing process is proposed and it has been proved that both the cation (Ca^{2+}) and anion (Cl^-) interact selectively with the polymers to promote the self-healing process: Ca^{2+} coordinates with PEOZ, and Cl^- coordinates with PHS in the form of hydrogen bonding. As a result, the synergistic effects among hydrogen bonds, metal–ligand coordination, and ionic bonds improve the healing rate and efficiency as well as mechanical strength to a certain extent. This hybrid material could potentially be used as a self-healable coating for the surfaces containing visual information or with optical functions, a repeatable adhesive with strong mechanical strength, and also as a conservation material for cultural heritage in both wet and ambient environments.

Conflicts of interest

There are no conflicts of interest to declare.

Acknowledgements

This research is supported by the National Natural Science Foundation of China (Grant No. 52072228), the Basic Research Fund for Free Exploration in Shenzhen (Grant No. JCYJ20180306171402878), the Project of Shaanxi Young Stars in Science and Technology (2017KJXX-18), the Shaanxi Provincial Key R&D Program (2020KWZ-018), and the Fundamental Research Funds for the Central Universities (3102019ghxm003, 3102019JC005, 3102019ghjd001). We thank Shaohua Dong

from Shaanxi Institute for the Preservation of Cultural Heritage for the help of micro-FTIR characterizations, and thanks to the Analytical & Testing Center of Northwestern Polytechnical University for the help in XPS characterization. We also appreciate Prof. Wei Tian and Xin Song from the School of Natural and Applied Sciences, Northwestern Polytechnical University for providing PEOZ ($M_w \sim 10{,}400$).

Notes and references

1 M. W. Urban, D. Davydovich, Y. Yang, T. Demir, Y. Zhang and L. Casabianca, *Science*, 2018, **362**, 220–225.
2 C. H. Li, C. Wang, C. Keplinger, J. L. Zuo, L. Jin, Y. Sun, P. Zheng, Y. Cao, F. Lissel, C. Linder, X. Z. You and Z. Bao, *Nat. Chem.*, 2016, **8**, 618–624.
3 Z. P. Zhang, M. Z. Rong and M. Q. Zhang, *Prog. Polym. Sci.*, 2018, **80**, 39–93.
4 T. P. Huynh, P. Sonar and H. Haick, *Adv. Mater.*, 2017, **29**, 1604973.
5 Y. Yang and M. W. Urban, *Chem. Soc. Rev.*, 2013, **42**, 7446–7467.
6 C. B. Highley, C. B. Rodell and J. A. Burdick, *Adv. Mater.*, 2015, **27**, 5075–5079.
7 S. Park, G. Thangavel, K. Parida, S. Li and P. S. Lee, *Adv. Mater.*, 2019, **31**, 1805536.
8 J. Kang, D. Son, G. N. Wang, Y. Liu, J. Lopez, Y. Kim, J. Y. Oh, T. Katsumata, J. Mun, Y. Lee, L. Jin, J. B. Tok and Z. Bao, *Adv. Mater.*, 2018, **30**, 1706846.
9 M. Liu, P. Liu, G. Lu, Z. Xu and X. Yao, *Angew. Chem., Int. Ed.*, 2018, **57**, 11242–11246.
10 S. Burattini, B. W. Greenland, D. H. Merino, W. Weng, J. Seppala, H. M. Colquhoun, W. Hayes, M. E. Mackay, I. W. Hamley and S. J. Rowan, *J. Am. Chem. Soc.*, 2010, **132**, 12051–12058.
11 R. Tepper, S. Bode, R. Geitner, M. Jager, H. Gorls, J. Vitz, B. Dietzek, M. Schmitt, J. Popp, M. D. Hager and U. S. Schubert, *Angew. Chem., Int. Ed.*, 2017, **56**, 4047–4051.
12 J. Fox, J. J. Wie, B. W. Greenland, S. Burattini, W. Hayes, H. M. Colquhoun, M. E. Mackay and S. J. Rowan, *J. Am. Chem. Soc.*, 2012, **134**, 5362–5368.
13 L. Li, B. Yan, J. Yang, L. Chen and H. Zeng, *Adv. Mater.*, 2015, **27**, 1294–1299.
14 Z. Jiang, M. L. Tan, M. Taheri, Q. Yan, T. Tsuzuki, M. G. Gardiner, B. Diggle and L. A. Connal, *Angew. Chem., Int. Ed.*, 2020, **59**, 7049–7056.
15 S. Lin, Y. Zhong, X. Zhao, T. Sawada, X. Li, W. Lei, M. Wang, T. Serizawa and H. Zhu, *Adv. Mater.*, 2018, **30**, 1803004.
16 C. Cui, T. Wu, F. Gao, C. Fan, Z. Xu, H. Wang, B. Liu and W. Liu, *Adv. Funct. Mater.*, 2018, **28**, 1804925.
17 Y.-L. Rao, A. Chortos, R. Pfattner, F. Lissel, Y.-C. Chiu, V. Feig, J. Xu, T. Kurosawa, X. Gu, C. Wang, M. He, J. W. Chung and Z. Bao, *J. Am. Chem. Soc.*, 2016, **138**, 6020–6027.
18 N. Kuhl, S. Bode, R. K. Bose, J. Vitz, A. Seifert, S. Hoeppener, S. J. Garcia, S. Spange, S. van der Zwaag, M. D. Hager and U. S. Schubert, *Adv. Funct. Mater.*, 2015, **25**, 3295–3301.
19 P. Reutenauer, E. Buhler, P. J. Boul, S. J. Candau and J. M. Lehn, *Chemistry*, 2009, **15**, 1893–1900.
20 A. M. Asadirad, S. Boutault, Z. Erno and N. R. Branda, *J. Am. Chem. Soc.*, 2014, **136**, 3024–3027.
21 O. R. Cromwell, J. Chung and Z. Guan, *J. Am. Chem. Soc.*, 2015, **137**, 6492–6495.
22 J. J. Cash, T. Kubo, A. P. Bapat and B. S. Sumerlin, *Macromolecules*, 2015, **48**, 2098–2106.
23 Y. Lai, X. Kuang, P. Zhu, M. Huang, X. Dong and D. Wang, *Adv. Mater.*, 2018, **30**, 1802556.
24 Z. Jiang, A. Bhaskaran, H. M. Aitken, I. C. G. Shackleford and L. A. Connal, *Macromol. Rapid Commun.*, 2019, **40**, 1900038.
25 Z. Jiang, B. Diggle, I. C. G. Shackleford and L. A. Connal, *Adv. Mater.*, 2019, **31**, 1904956.
26 J. Collins, M. Nadgorny, Z. Xiao and L. A. Connal, *Macromol. Rapid Commun.*, 2017, **38**, 1600760.
27 B. Zhang, Z. A. Digby, J. A. Flum, E. M. Foster, J. L. Sparks and D. Konkolewicz, *Polym. Chem.*, 2015, **6**, 7368–7372.
28 T. Wang, Y. Zhang, Q. Liu, W. Cheng, X. Wang, L. Pan, B. Xu and H. Xu, *Adv. Funct. Mater.*, 2018, **28**, 1705551.
29 Y. Zhang, L. Yuan, G. Liang and A. Gu, *J. Mater. Chem. A*, 2018, **6**, 23425–23434.
30 Z. Xiang, L. Zhang, Y. Li, T. Yuan, W. Zhang and J. Sun, *ACS Nano*, 2017, **11**, 7134–7141.
31 J. Liu, W. Duan, J. Song, X. Guo, Z. Wang, X. Shi, J. Liang, J. Wang, P. Cheng, Y. Chen, M. J. Zaworotko and Z. Zhang, *J. Am. Chem. Soc.*, 2019, **141**, 12064–12070.
32 J. Li, H. Ejima and N. Yoshie, *ACS Appl. Mater. Interfaces*, 2016, **8**, 19047–19053.
33 X. Qi, L. Yang, J. Zhu, Y. Hou and M. Yang, *ACS Nano*, 2016, **10**, 9434–9445.
34 A. Faghihnejad, K. E. Feldman, J. Yu, M. V. Tirrell, J. N. Israelachvili, C. J. Hawker, E. J. Kramer and H. Zeng, *Adv. Funct. Mater.*, 2014, **24**, 2322–2333.
35 X. Wang, Y. Li, Y. Qian, H. Qi, J. Li and J. Sun, *Adv. Mater.*, 2018, **30**, 1803854.
36 Q. Zhang, C.-Y. Shi, D.-H. Qu, Y.-T. Long, B. L. Feringa and H. Tian, *Sci. Adv.*, 2018, **4**, eaat8192.
37 S. Wang, Z. Liu, L. Zhang, Y. Guo, J. Song, J. Lou, Q. Guan, C. He and Z. You, *Mater. Chem. Front.*, 2019, **3**, 1833–1839.
38 C.-H. Li and J.-L. Zuo, *Adv. Mater.*, 2020, **32**, 1903762.
39 S. Bode, M. Enke, R. K. Bose, F. H. Schacher, S. J. Garcia, S. van der Zwaag, M. D. Hager and U. S. Schubert, *J. Mater. Chem. A*, 2015, **3**, 22145–22153.
40 Y.-L. Rao, V. Feig, X. Gu, G.-J. Nathan Wang and Z. Bao, *J. Polym. Sci., Part A: Polym. Chem.*, 2017, **55**, 3110–3116.
41 L. Shi, H. Carstensen, K. Hölzl, M. Lunzer, H. Li, J. Hilborn, A. Ovsianikov and D. A. Ossipov, *Chem. Mater.*, 2017, **29**, 5816–5823.
42 H. Meng, P. Xiao, J. Gu, X. Wen, J. Xu, C. Zhao, J. Zhang and T. Chen, *Chem. Commun.*, 2014, **50**, 12277–12280.
43 N. Roy, B. Bruchmann and J. M. Lehn, *Chem. Soc. Rev.*, 2015, **44**, 3786–3807.
44 R. Hoogenboom, M. W. M. Fijten, R. M. Paulus, H. M. L. Thijs, S. Hoeppener, G. Kickelbick and U. S. Schubert, *Polymer*, 2006, **47**, 75–84.

45 N. Schmid, A. P. Eichenberger, A. Choutko, S. Riniker, M. Winger, A. E. Mark and W. F. van Gunsteren, *Eur. Biophys. J.*, 2011, **40**, 843–856.
46 H. J. C. Berendsen, D. van der Spoel and R. van Drunen, *Comput. Phys. Commun.*, 1995, **91**, 43–56.
47 K. B. Koziara, M. Stroet, A. K. Malde and A. E. Mark, *J. Comput.-Aided Mol. Des.*, 2014, **28**, 221–233.
48 D. Sun, T. Lin, X. Zhu, Y. Tian and F. Liu, *Comput. Mater. Sci.*, 2016, **114**, 86–93.
49 Z. Wei, J. H. Yang, J. Zhou, F. Xu, M. Zrinyi, P. H. Dussault, Y. Osada and Y. M. Chen, *Chem. Soc. Rev.*, 2014, **43**, 8114–8131.
50 R. Merindol, S. Diabang, O. Felix, T. Roland, C. Gauthier and G. Decher, *ACS Nano*, 2015, **9**, 1127–1136.
51 X.-C. Chen, K.-F. Ren, J.-H. Zhang, D.-D. Li, E. Zhao, Z. J. Zhao, Z.-K. Xu and J. Ji, *Adv. Funct. Mater.*, 2015, **25**, 7470–7477.
52 W. Guo, X. Li, F. Xu, Y. Li and J. Sun, *ACS Appl. Mater. Interfaces*, 2018, **10**, 13073–13081.
53 T. L. Sun, T. Kurokawa, S. Kuroda, A. B. Ihsan, T. Akasaki, K. Sato, M. A. Haque, T. Nakajima and J. P. Gong, *Nat. Mater.*, 2013, **12**, 932–937.
54 D. Lin-Vien, N. B. Colthup, W. G. Fateley and J. G. Grasselli, *Aromatic and Heteroaromatic Rings*, Elsevier Science, 1991, ch. 17, p. 281.
55 L. Xu, E. Yokoyama and M. Satoh, *Langmuir*, 2005, **21**, 7153–7160.
56 R. Sudarshan, G. R. Rao and V. V. Chalapathi, *J. Raman Spectrosc.*, 1990, **21**, 407–415.
57 G. Durgaprasad, D. N. Sathyanarayana, C. C. Patel, H. S. Randhawa, A. Goel and C. N. R. Rao, *Spectrochim. Acta, A*, 1972, **28**, 2311–2318.
58 J. Wang, M. K. Cheung and Y. Mi, *Polymer*, 2001, **42**, 2077–2083.
59 J. S. Klitzke, T. Roisnel, E. Kirillov, O. D. L. Casagrande and J.-F. Carpentier, *Organometallics*, 2013, **33**, 309–321.
60 X. Li, M. Ibrahim Dar, C. Yi, J. Luo, M. Tschumi, S. M. Zakeeruddin, M. K. Nazeeruddin, H. Han and M. Grätzel, *Nat. Chem.*, 2015, **7**, 703–711.
61 J. R. Ebner, D. L. McFadden, D. R. Tyler and R. A. Walton, *Inorg. Chem.*, 1976, **15**, 3014–3018.
62 D. K. Smith, *Org. Biomol. Chem.*, 2003, **1**, 3874–3877.
63 M. Zhong, Y.-T. Liu and X.-M. Xie, *J. Mater. Chem. B*, 2015, **3**, 4001–4008.
64 F. Byette, A. Laventure, I. Marcotte and C. Pellerin, *Biomacromolecules*, 2016, **17**, 3277–3286.
65 D. Chelazzi, R. Giorgi and P. Baglioni, *Angew. Chem., Int. Ed.*, 2018, **57**, 7296–7303.
66 C. Dang, M. Wang, J. Yu, Y. Chen, S. Zhou, X. Feng, D. Liu and H. Qi, *Adv. Funct. Mater.*, 2019, **29**, 1902467.
67 X. Qi, Y. Hou and M. Yang, *Adv. Funct. Mater.*, 2019, **29**, 1903984.
68 C. Cui, T. Wu, F. Gao, C. Fan, Z. Xu, H. Wang, B. Liu and W. Liu, *Adv. Funct. Mater.*, 2018, **28**, 1804925.
69 S. M. Kim, H. Jeon, S. H. Shin, S. A. Park, J. Jegal, S. Y. Hwang, D. X. Oh and J. Park, *Adv. Mater.*, 2018, **30**, 1705145.
70 C. Shao, M. Wang, L. Meng, H. Chang, B. Wang, F. Xu, J. Yang and P. Wan, *Chem. Mater.*, 2018, **30**, 3110–3121.
71 Z. Zhang, Z. Gao, Y. Wang, L. Guo, C. Yin, X. Zhang, J. Hao, G. Zhang and L. Chen, *Macromolecules*, 2019, **52**, 2531–2541.
72 J. Qu, X. Zhao, Y. Liang, T. Zhang, P. X. Ma and B. Guo, *Biomaterials*, 2018, **183**, 185–199.
73 X. Jing, H. Y. Mi, Y. J. Lin, E. Enriquez, X. F. Peng and L. S. Turng, *ACS Appl. Mater. Interfaces*, 2018, **10**, 20897–20909.
74 H. Fan, J. Wang and Z. Jin, *Macromolecules*, 2018, **51**, 1696–1705.
75 L. Han, L. Yan, K. Wang, L. Fang, H. Zhang, Y. Tang, Y. Ding, L.-T. Weng, J. Xu, J. Weng, Y. Liu, F. Ren and X. Lu, *NPG Asia Mater.*, 2017, **9**, e372.
76 R. Chen, X. Xu, D. Yu, M. Liu, C. Xiao, I. Wyman, Z. Wang, H. Yang and X. Wu, *NPG Asia Mater.*, 2019, **11**, 22.
77 J. Chen, J. Liu, T. Thundat and H. Zeng, *ACS Appl. Mater. Interfaces*, 2019, **11**, 18720–18729.